Physica Medica 42 (2017) 162–173

Contents lists available at ScienceDirect

Physica Medica

journal homepage: www.elsevier.com/locate/ejmp

Original paper

Medical image segmentation based on level set and isoperimetric constraint

Luying Gui[a], Chunming Li[b], Xiaoping Yang[c,*]

[a] The Department of Mathematics, Nanjing University of Science and Technology, Nanjing, Jiangsu 210094, China
[b] The School of Electronic Engineering, University of Electronic Science and Technology of China, Chengdu, Sichuan 611731, China
[c] The Department of Mathematics, Nanjing University, Nanjing, Jiangsu 210093, China

ARTICLE INFO

Keywords:
Lesion segmentation
Level set
Isoperimetric constraint
Compact shapes
Blurred or/and partially missing boundaries

ABSTRACT

Level set based methods are being increasingly used in image segmentation. In these methods, various shape constraints can be incorporated into the energy functionals to obtain the desired shapes of the contours represented by their zero level sets of functions. Motivated by the isoperimetric inequality in differential geometry, we propose a segmentation method in which the isoperimetric constrain is integrated into a level set framework to penalize the ratio of its squared perimeter to its enclosed area of an active contour. The new model can ensure the compactness of segmenting objects and complete missing or/and blurred parts of their boundaries simultaneously. The isoperimetric shape constraint is free of explicit expressions of shapes and scale-invariant. As a result, the proposed method can handle various objects with different scales and does not need to estimate parameters of shapes. Our method can segment lesions with blurred or/and partially missing boundaries in ultrasound, Computed Tomography (CT) and Magnetic Resonance (MR) images efficiently. Quantitative evaluation also confirms that the proposed method can provide more accurate segmentation than two well-known level set methods. Therefore, our proposed method shows potential of accurate segmentation of lesions for applying in diagnoses and surgical planning.

1. Introduction

Images segmentation performs an important function in medical image processing and analysis [1–4]. However, there are challenges in segmentation due to the presence of noise, low contrast, inhomogeneity, blurred or/and partially missing boundaries and image artifacts in medical images [5–7]. To overcome these difficulties, prior knowledge, such as shape priors [8–13], texture priors [8], appearances priors [14], and statistic priors [15–18], has been used to segment lesions and organs in medical image segmentation.

Level set based methods are powerful and efficient methodologies for image segmentation [19,20]. In particular, they have been successfully applied in the segmentation of medical images [16,18,21–23]. In these methods, a contour is represented as the zero level set of a function. The desired shape of the contour can be controlled by a regularization term (e.g. a shape prior constraint) in the energy functional [24].

The shape prior is a kind of commonly used prior knowledge for segmentation. There are two main approaches to obtain various kinds of shape priors, i.e. training and analytical expressions of shapes. Chen et al. [25] proposed a method to implement in cardiac ultrasound images and functional MR images for corpus callosum segmentation by incorporating a shape prior into a geometric active contour model. In their method, a large number of samples were used in training to obtain a proper shape prior. Leventon et al. [26] employed a trained curvature as prior information for segmenting joint and corpus callosum in MR images. Although the trained shape priors significantly facilitate segmentation, the procedure of training is time consuming. In addition, the final segmentation results are affected by the number and selection of trained samples.

The analytic expression of shapes, such as the equations of circles and ellipses, can be implemented as shape constrains. Because the variations for shapes of objects should be considered in segmentation, shape prior expressions are usually defined in terms of transformations from given shape templates [25]. In this case, the boundaries of objects are obtained by optimizing the parameters of shape transformations including scales, rotations and shifts, so that transformed templates can better fit the real boundaries of objects. Acton et al. [24] proposed a novel method to track the movement of leukocytes and to locate the target cells by using the constraints of shape and size. They used ellipses as shape priors, and five parameters were used to control the shape energy term.

In this paper, a novel shape constraint is proposed for handling a type of shapes, which are called compact shapes. The new shape

* Corresponding author.
E-mail addresses: guiluying@hotmail.com (L. Gui), li_chunming@hotmail.com (C. Li), yangxp@njust.edu.cn (X. Yang).

http://dx.doi.org/10.1016/j.ejmp.2017.09.123
Received 2 March 2017; Received in revised form 16 August 2017; Accepted 13 September 2017
Available online 30 September 2017

constraint does not rely on any trained prior or parameter selection and estimation, and therefore has good usability in applications. Many lesions and organs (e.g. most renal carcinomas, cysts, breast cancers, nodules as well as cells, kidneys and prostates) in medical images exhibit compact shapes that are quasi-circles, quasi-ellipses and their variants. For instance, the nodular type of hepatic cellular cancer (HCC) regions that are divided into three categories according to their morphological appearances [27] can be regarded as compact shapes. The proposed segmentation method based on our novel shape constraint can therefore be widely used in clinical applications. Accurate segmentation of the organs and lesions in medical images is of great significance. The segmentation results provide precise measurements of these regions, which can be used in the subsequent processes including diagnoses, analysis, and therapy planning. Traditional segmentation is achieved manually. However, this labor-intensive work consumes a lot of time. Moreover, the accuracies of the results are largely depend on the experiences of the operators. Additionally, the nonrepeatability of the results brings inconveniences for the subsequent procedures. In order to reduce the workload and strengthen clinical applications, accurate and robust segmentation methods are necessary in medical image processing. For example, an HCC with a diameter less than 3 cm that is considered small [28], can be effectively cured by percutaneous ethanol injection instead of surgical resection that would be necessary for bigger HCCs [29]. Moreover, precise segmentation results can delineate the boundaries of lesions, which provide the accurate target regions for radiofrequency ablation and radiation therapy. The accurate segmentation results can also be used in comparison of the preoperative and postoperative regions, and the therapeutic evaluation can be acquired precisely.

The proposed shape constraint, called the isoperimetric constraint, is motivated by the well-known isoperimetric inequality in differential geometry. This constraint is based on the ratio of its squared perimeter to the enclosed area of an active contour, and acts as an efficient regularization term. The isoperimetric constraint in the proposed model is integrated into a level set based segmentation scheme. The new model has advantages in three aspects. Firstly, under the isoperimetric constraint, the active contour tends to move to the boundary of a compact shape, which is beneficial for segmenting some lesions and organs in medical images. Moreover, this function is established by the by controlling the ratio of square length to the area, under this circumstance, the smoothness of the contour are ensured. Secondly, the proposed model has an inherent mechanism of completing the missing or/and blurred parts of the boundaries, because the isoperimetric constraint effectively controls the perimeter and the area of a shape at the same time. In other words, the constraint forces the active contour to enclose a compact region and therefore to draw up the objects that even have blurred or/and partially missing boundaries. Thirdly, the isoperimetric constraint is scale invariant. This fact means that the proposed model can handle objects with different sizes and is free of estimating the parameters of shapes.

The proposed model is validated by experiments of segmenting various objects including lesions, organs and structures in different medical images that suffer from noises, inhomogeneities, and blurred or/and partially missing boundaries. In addition, the proposed method is compared with other two well-known level set methods. The average precision and the average Dice coefficient of the proposed method in both ultrasound images and CT images are higher than other two efficient segmentation methods. Experimental results and quantitative analyses indicate that the proposed method can provide the best segmentation results among all the tested methods.

2. Problem formulation

In image segmentation, the length of a contour is one of the most commonly used regularization terms for level set methods. Among all of these methods, the classical Chan-Vese (CV) model [30] is a typical example, in which the arc length of the active contour is adopted as a regularization term. The general form of the CV model is represented as follows:

$$F(C) = E_{data} + Length(C), \tag{1}$$

where C is the active contour; E_{data} is the data term (the fitting term) that forces the contour to close the real boundaries of objects; and the length term (the regularization term) $Length(C)$ controls the smoothness of the active contour. However, this length term may be unable to maintain enough properties for segmenting objects in some complex situations. For instance, in a low-contrast image that is also contaminated by heavy noises, an object is always confused by the background nearby. To tackle such an image, a regularization term with more prior information is needed.

In recent years, various shape constraints are employed as effective regularization terms. Motivated by the isoperimetric inequality in differential geometry, we propose a novel shape constraint and integrate it into a level set framework to efficiently segment compact regions with blurred or/and partially missing boundaries in medical images. The isoperimetric inequality for any bounded Lipschitz domain $\Omega \in R^n, n \geqslant 2$, can be represented as follows [31]:

$$\frac{|\partial\Omega|}{|\Omega|^{\frac{n-1}{n}}} \geqslant n^{\frac{n-1}{n}} C_{n-1}^{\frac{1}{n}}, \tag{2}$$

where $C_{n-1} = \frac{2\pi^{n/2}}{\Gamma(n/2)}$ is called the isoperimetric constant; $\partial\Omega$ is the boundary of the domain Ω and of Lipschitz; and $|\partial\Omega|$ and $|\Omega|$ are the surface measure and volume measure of $\partial\Omega$ and Ω, respectively.

As is well known, in two-dimensional (2D) cases, the shape of Ω is close to a round when the ratio $\frac{|\partial\Omega|}{|\Omega|^{1/2}}$ is close to the isoperimetric constant $2C^{1/2}$. For two regions Ω_1 and Ω_2, if $\frac{|\partial\Omega_1|}{|\Omega_1|^{1/2}} < \frac{|\partial\Omega_2|}{|\Omega_2|^{1/2}}, \frac{|\partial\Omega_1|}{|\Omega_1|^{1/2}}$ is closer to the isoperimetric constant, which means that Ω_1 can be considered to be more compact than Ω_2. In other words, small value of the ratio of a shape indicates that it appears relatively compact. Based on this observation, we calculate the value of $(|\partial\Omega|^2/4\pi|\Omega|)^p$ (also written as $(L^2/4\pi A)^p$) called the $AP-ratio$ to quantitatively characterize compactness. In order to better illustrate the compactness characterization, we calculate the $AP-ratio$ with different values of the parameter p for a series of ellipses with gradual changes of long axis/short axis ratios. As seen in Fig. 1, the $AP-ratio$ rises as the 'long axis/short axis' ratio increases. In addition, the comparison between Fig. 1(a) and (b) indicates that a larger value of the parameter p leads to a faster increase of the $AP-ratio$.

The concept of compactness has been proposed as the prior knowledge in some previous segmentation models. Veksler et al. [32] adopted the ratio of the perimeter to the area ($\frac{L}{A}$) of an object to define its compactness in their segmentation model. Grady et al. [33] employed this compactness concept to describe the shape priors and segmented images by minimizing the ratio $h = \frac{L}{A}$ (in two-dimensional space) under a graph partitioning framework. This graph based method has been used to segment heart chambers in cardiovascular imaging [34], aortic cross-section [35], and unknown objects for baggage security [36]. Koepfler et al. [37] used the similar description of compactness for segmentation. In order to realize the segmentation by region merging, they proposed a merging criterion based on the isoperimetric inequality to eliminate small regions and thin regions.

In this paper, we use the $AP-ratio$: $(L^2/4\pi A)^p$ to describe the compactness of a shape. The $AP-ratio$ is different from the ratio of L/A. The $AP-ratio$ is scale-invariance, for example, different sizes of circles have the same value of the $AP-ratios$, this property is reasonable and important because of the fact that even the same lesions and organs may present different sizes in different times. On the contrary, the value of the ratio L/A decreases as the radii of a circle increases. As a shape constraint, this $AP-ratio$ is embedded into a level set framework. The smoothness and the compactness of the segmented regions are guaranteed by the proposed constraint.

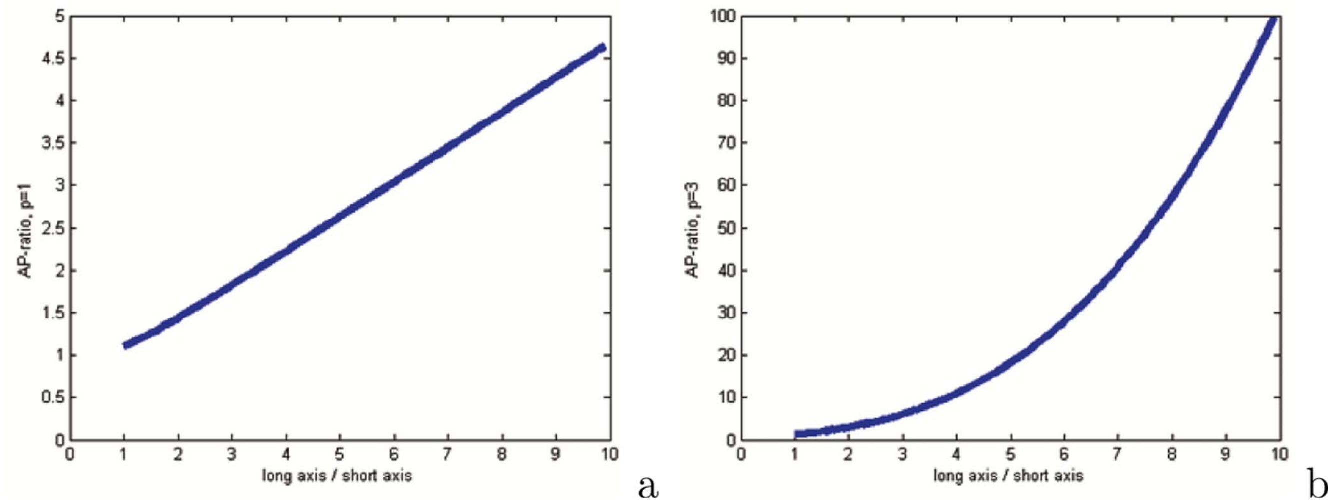

Fig. 1. The $AP-ratios$ for different ratios of 'long axis/short axis' in ellipses. a: p = 1, b: p = 3.

3. Method

3.1. Description of the proposed model

According to the $AP-ratio$, we propose an energy term of shape constraint as follows:

$$E_{shape}(C) = \left(\frac{length(C)^2}{4\pi Area(inside(C))}\right)^p, \tag{3}$$

where p is a positive constant, which is related to strength of the shape constraint. The selection of p is a trade-off problem. We determine the proper range of p for further segmentation by using a series experiments that are described in Section 4.2. The shape energy is combined with a data term to formulate an energy functional for segmentation:

$$E = \theta E_{shape} + E_{data} \quad (\theta > 0), \tag{4}$$

where θ is a constant controlling the effect of E_{shape}, and E_{data} is a data term defined in the CV model [30].

Thus, the energy functional (6) can be defined as follows:

$$E(c_1,c_2,C) = \theta\left(\frac{L(C)^2}{4\pi A(inside(C))}\right)^p + \lambda_1 \int_{inside(C)} |u_0(x,y)-c_1|^2 dxdy + \lambda_2 \int_{outside(C)} |u_0(x,y)-c_2|^2 dxdy. \tag{5}$$

In this functional, $u_0(x,y)$ is the gray level of the pixel (x,y) in an image u_0;C is the active contour; c_1 and c_2 are the averages of $u_0(x,y)$ inside C and outside C, respectively; and $\theta,\lambda_1,\lambda_2 > 0$ control the trade-off between the shape term and intensity terms. The proposed E_{shape} acts as a regularization term, and is also an implicit requirement of smoothness for C. For two given contours C^1 and C^2, if $E_{shape}(C^1) < E_{shape}(C^2)$, it can be deduced that $\frac{L^2}{A}(C^1) < \frac{L^2}{A}(C^2)$, considering the exponent $p > 0$. If $A(inside(C^1))$ is equal to $A(inside(C^2))$,$L(C^1)$ is then smaller than $L(C^2)$, which means the contour C^1 is smoother than the contour C^2, while the shape of a region inside C^1 is more compact than that inside C^2. Thus the regularization term adjusts the shapes and smoothness of active contours. The second term and third term in (5) are fitting terms that encourage a contour to approach to the real boundary of an object. Therefore, we can acquire the optimal contour by solving the energy minimization problem as follows:

$$\min_{c_1,c_2,C} E(c_1,c_2,C).$$

3.2. Level Set Formulation of the Model

In order to solve this problem, a level set function for a given open domain Ω in R^2 can be defined as described in [38]:

$$\phi(x,y)\begin{cases} >0 & for\ (x,y) \in \Omega, \\ =0 & for\ (x,y) \in \partial\Omega, \\ <0 & for\ (x,y) \notin (\Omega \bigcup \partial\Omega). \end{cases} \tag{6}$$

In (6), the boundary $\partial\Omega$ is represented by the zero level set of ϕ. In order to reformulate the energy functional $E(c_1,c_2,C)$, we introduce the heaviside function H, and the one-dimensional Dirac measure (in the distribution sense), which are defined by:

$$H(s) = \begin{cases} 1 & if\ s \geqslant 0, \\ 0 & if\ s < 0. \end{cases}, \delta(s) = \frac{d}{ds}H(s). \tag{7}$$

Then, the energy $E(c_1,c_2,C)$ can be rewritten as:

$$E(c_1,c_2,\phi) = \theta\left(\frac{(\int_\Omega \delta(\phi(x,y))|\nabla\phi(x,y)|dxdy)^2}{4\pi\int_\Omega H(\phi(x,y))dxdy}\right)^p + \lambda_1 \int_\Omega |u_0(x,y) - c_1|^2 H(\phi(x,y))dxdy + \lambda_2 \int_\Omega |u_0(x,y) - c_2|^2 (1-H(\phi(x,y)))dxdy. \tag{8}$$

In order to compute the associated Euler–Lagrange equation, we introduce a regularized version H_ϵ of the function H, and its derivative δ_ϵ as follows:

$$H_\epsilon(s) = \frac{1}{2}\left(1 + \frac{2}{\pi}\arctan\left(\frac{s}{\epsilon}\right)\right),$$

and

$$\delta_\epsilon(s) = \frac{1}{\pi}\cdot\frac{\epsilon}{\epsilon^2 + s^2}.$$

Then, the Euler - Lagrange equation for ϕ is:

$$\frac{\partial\phi}{\partial t} = K\cdot\delta_\epsilon(\phi)\left[L + 2A\cdot div\left(\frac{\nabla\phi}{|\nabla\phi|}\right)\right] + \delta_\epsilon(\phi)[-\lambda_1(u_0-c_1)^2 + \lambda_2(u_0-c_2)^2], \tag{9}$$

where

$$K = \frac{\theta p L^{2p-1}}{(4\pi)^p A^{p+1}}. \tag{10}$$

3.3. Numerical Scheme

We adopt the following finite differences:

$$\triangle_-^x\phi_{i,j} = \phi_{i,j}-\phi_{i-1,j},\quad \triangle_+^x\phi_{i,j} = \phi_{i+1,j}-\phi_{i,j},$$
$$\triangle_-^y\phi_{i,j} = \phi_{i,j}-\phi_{i,j-1},\quad \triangle_+^y\phi_{i,j} = \phi_{i,j+1}-\phi_{i,j}.$$

Then, the Eq. (9) is discretized to:

$$\frac{\phi_{i,j}^{n+1}-\phi_{i,j}^{n}}{\triangle t} = K\cdot\delta_h(\phi_{i,j}^n)\Bigg[\frac{2A}{h^2}\triangle_-^x\cdot\left(\frac{\triangle_+^x\phi_{i,j}^{n+1}}{\sqrt{(\triangle_+^x\phi_{i,j}^n)^2/(h^2)+(\phi_{i,j+1}^n-\phi_{i,j-1}^n)^2/(2h)^2}}\right)$$
$$+\frac{2A}{h^2}\triangle_-^y\cdot\left(\frac{\triangle_+^y\phi_{i,j}^{n+1}}{\sqrt{(\triangle_+^y\phi_{i,j}^n)^2/(h^2)+(\phi_{i+1,j}^n-\phi_{i-1,j}^n)^2/(2h)^2}}\right)+L$$
$$-\lambda_1(u_{0,i,j}-c_1(\phi^n))^2+\lambda_2(u_{0,i,j}-c_2(\phi^n))^2\Bigg], \tag{11}$$

where h is a space step, and $\triangle t$ is a time step. The linear system (11) can be solved by using an iterative method with a given initial level set function ϕ^0.

4. Results

In order to validate the efficiency of the proposed method, experiments on synthetic images and medical images are carried out. Fig. 2. shows results of experiments on synthetic images. The results indicate that the proposed compact constraint has different impacts on objects with different degrees of compactness. In these tests, we use two objects, one is an ellipse and another one is an irregular shape as shown in Fig. 2. We increase the value of the perimeter p and obtain different segmentation results by using the proposed method. Results of segmenting those two objects for $p = 2, p = 2.5, p = 3, p = 3.5$ are presented. Because it is relatively compact, the ellipse object acquires four similar results for different values of p. However, the irregular shape object acquires different results for different values of p. From the results of the irregular shape object, we can see that the segmented shapes become more compact as the values of p become large. This indicates that the shape constraint has less impact for smaller p. However, the shape constraint becomes strong if the value of p increases. As a result, the active contour tends to enclose a more compact region for large p. These results confirm that the isoperimetric constraint imposes a stronger penalty on the less compact shapes.

Experimental results for segmenting lesions and tissues in medical images are also presented in this section. These lesions and tissues include renal lesions, thyroid nodules and cervical vessels in ultrasound images, HCCs in CT images and some organs and structures. To achieve effective segmentation, suitable value ranges of the parameter p related to ultrasound and CT images are discussed respectively. Efficiency of our proposed model is confirmed by quantitatively evaluating a series experiments and comparing with two well known level set based methods [30,39].

4.1. Initializations for segmentation

For renal cyst regions, we design an automatic detection approach to extract the rough regions of targets based on the fact that renal cysts in ultrasound images exhibit round shapes, anechoic features and relatively even distributions of gray level [40].

This detection procedure has two steps. Taking an ultrasound image as example, the original image is shown in Fig. 3a, the result of each step is shown in Fig. 3b–e. In the first step, the Otsu algorithm [41] is implemented twice to separate the dark regions of images as potential targets. In the first implementation of the Otsu algorithm, dark regions in images can be extracted as primary targets and the result obtained by this operation is shown in Fig. 3b. However, as a result of this global threshold, some of those extracted dark regions may be incompact and irregular, as well as exhibiting uneven intensity distribution. Therefore, the Otsu algorithm is implemented again on every one of these regions, to obtain the finer potential targets and the result obtained is shown in Fig. 3c. In the second step, real targets (renal cysts) are selected from the potential targets based on their sonographic characters of round shapes, posterior acoustic enhancements, anechoic and homogeneous regions. Artifacts and shadows with dark appearances usually exhibit inhomogeneous intensities, non-circular shapes, and have no posterior acoustic enhancements [40], so that they are distinct from the real targets. For the exhibited example, the selected target region is shown in Fig. 3d.

Considering that the detected results may be affected by undesired factors such as blurred edges and partially missing boundaries, and such influences can reduce the accuracy in further segmentation. A smaller

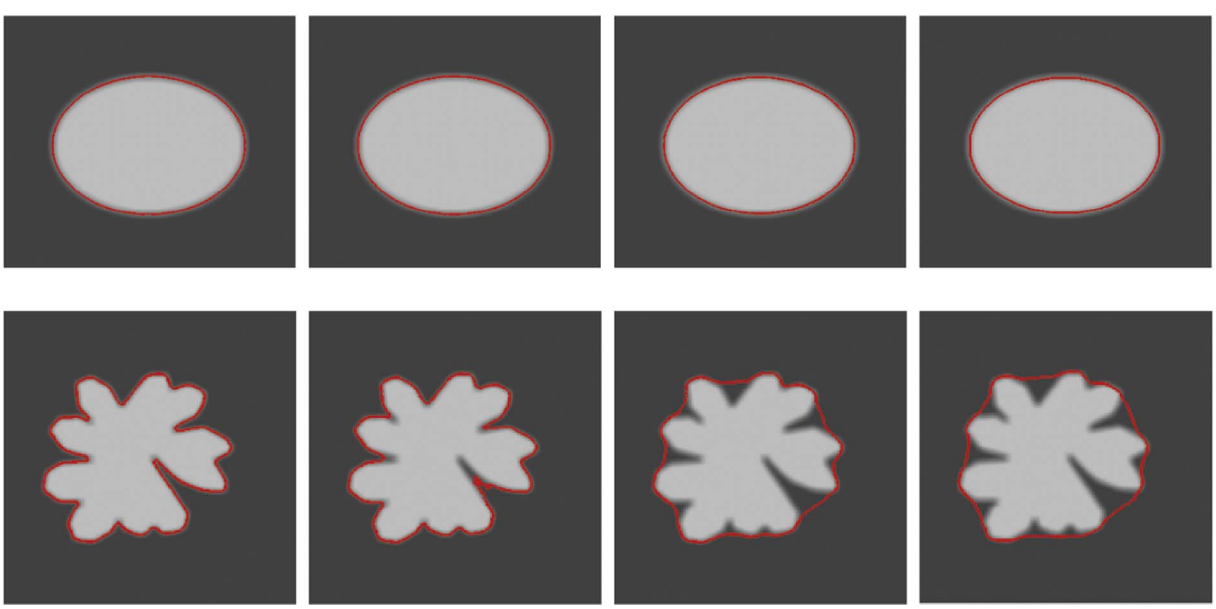

Fig. 2. Segmentation results of synthetic images with ellipse and irregular objects, respectively. From left to right: the values of p are 2, 2.5, 3 and 3.5. For all images, the iteration numbers are same.

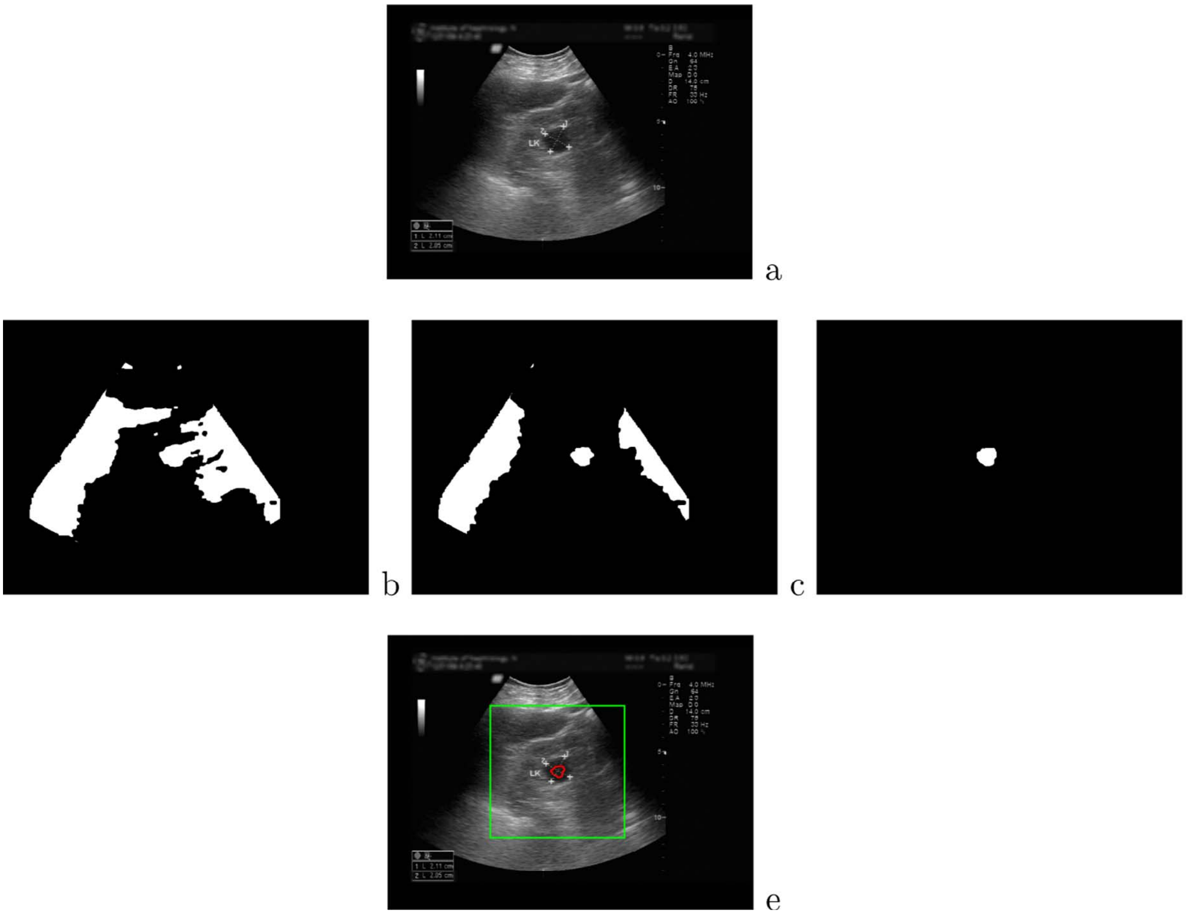

Fig. 3. a: the original ultrasound image; b: result obtained by the first implementation of Otsu thresholding; c: result obtained by the second implementation of Otsu thresholding; d: the target region selected from these isolated regions based on the acoustic characters of the cystic lesions; e: the automatically generated initial curve (red) and the processing regions (green). (For interpretation of the references to colour in this figure legend, the reader is referred to the web version of this article.)

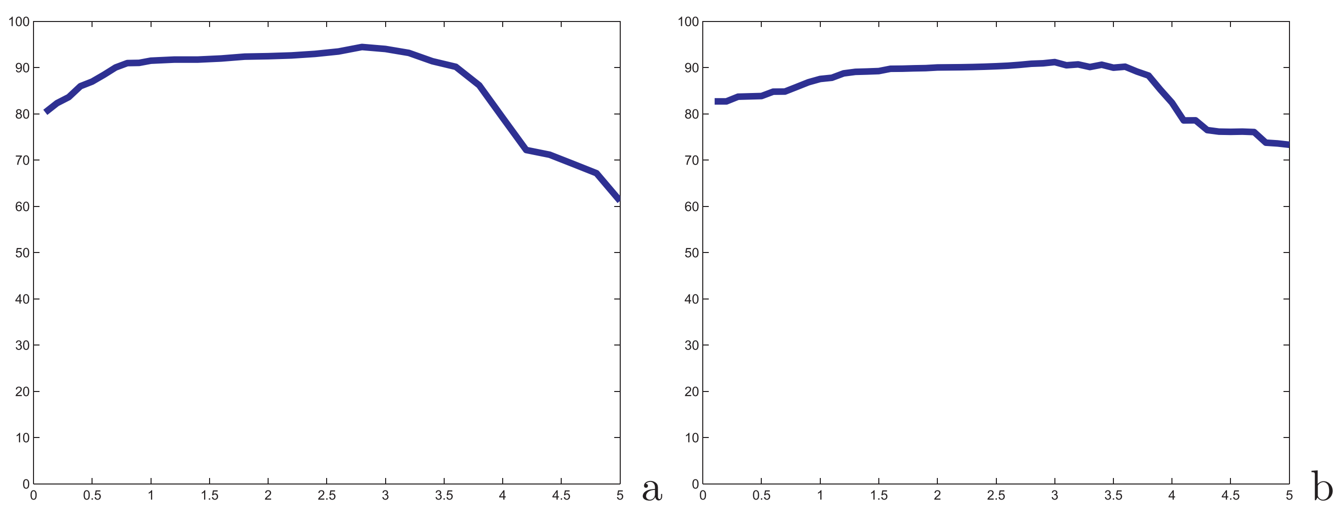

Fig. 4. Average Dice of the segmentation results for (a): 20 ultrasound images and (b): 20 CT images using different values of p in the interval [0.1,5].

initialization region can reduce the risk of being affected by these negative factors. Therefore, after detecting the real targets, an erosion operator is implemented on these regions to obtain the narrowed regions, and the boundaries of these narrowed regions are taken as the initial contours for the subsequent segmentation. In order to reduce time consumption and increase accuracy, a rectangular neighbourhood of the real target is automatically generated based on the detection result as the processing regions, i.e., all the computations in the segmentation process are applied on these regions. To generate a large enough processing region, a dilate operator is implemented on the detected target region. After that, a bounding box of the expanded region is taken, and the enclosed area is the processing region. In Fig. 3e, the red contour is the initial contour, and the green rectangular contour indicates the processing region.

Since some types of thyroid nodules, arteries, and renal carcinomas in ultrasound images exhibit similar sonographic characters, the above

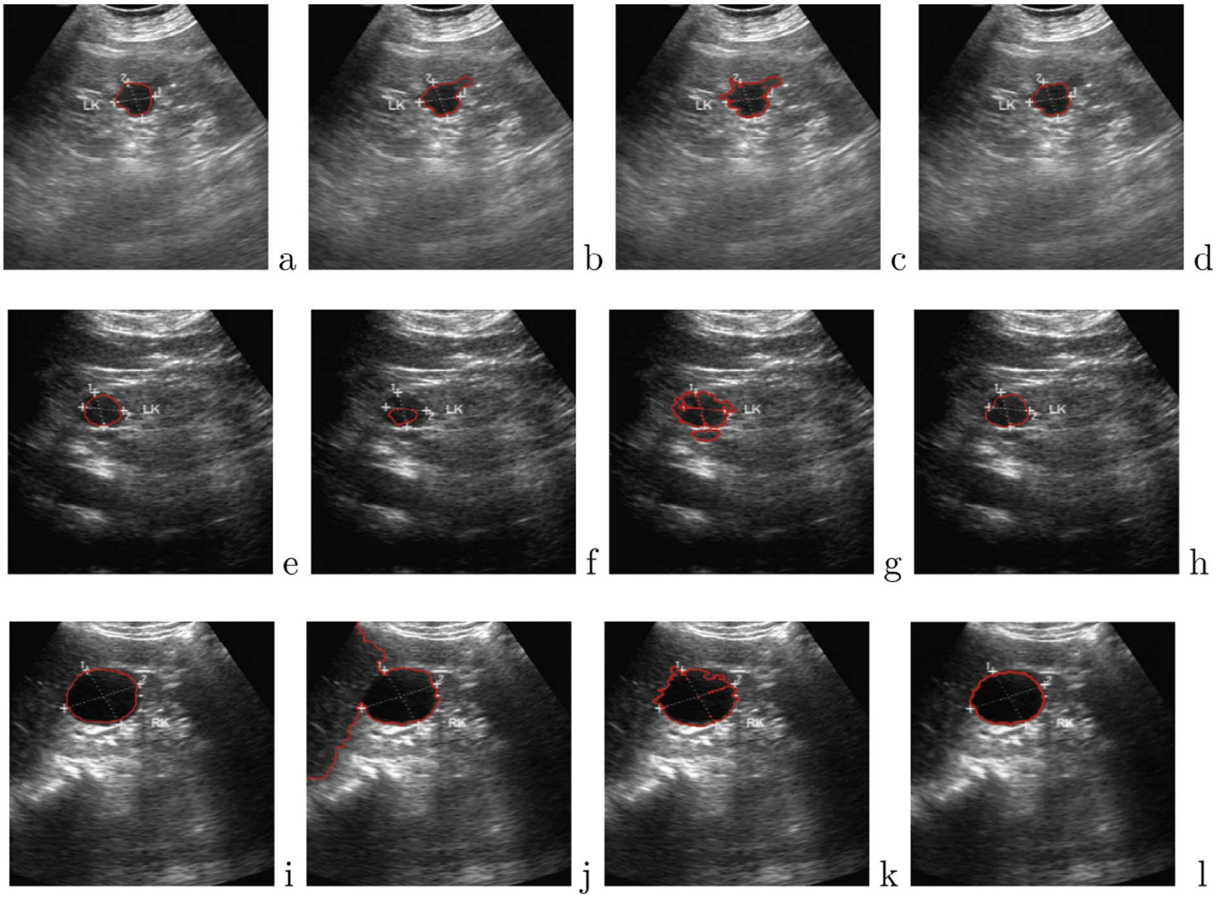

Fig. 5. Segmentation results of CV model, BCS method and the proposed method on the ultrasound images of renal cysts with blurred or/and partially missing boundaries. Automatically acquired initializations and processing region are used for all methods in this comparison. The 1st. column: the ground truths; the 2nd. column: the results of the CV model; the 3rd. column: the results of the BCS method; the 4th. column: the results of our proposed method.

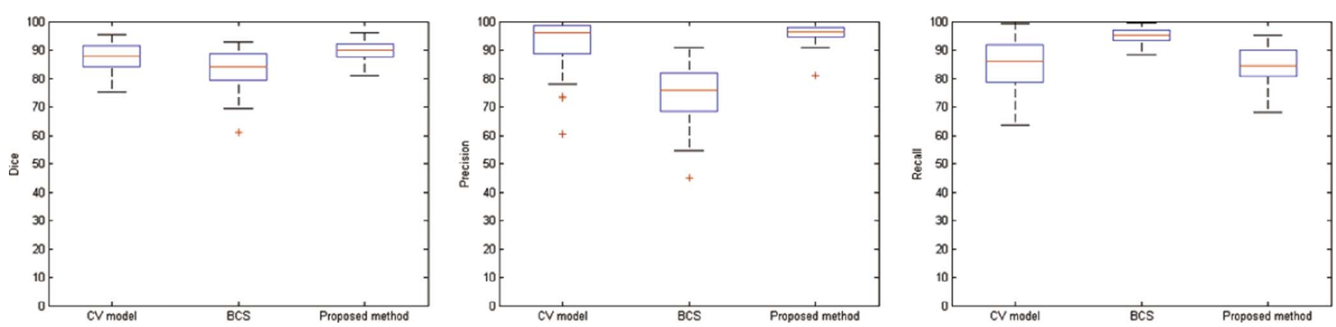

Fig. 6. The results of Dice, precision and recall (sensitivity). The CV model, the BCS method and the proposed method are compared. 52 ultrasound images with renal cysts are tested in this experiment.

automatic initialization can also be utilized for their segmentation as well. However, the lesions without these sonographic features, such as HCC regions in CT images, have to be manually initialized (see Fig. 7).

4.2. Selection of parameter p

In the proposed method, the parameter p determines the strength of the novel shape constraint and consequently affects the accuracy of segmentation results. Small values of p that imply small constraints may cause segmentation leakage results. On the contrary, strong constraints that are caused by large values of p likely cause erroneous segmentation results. Therefore, a proper value of p is necessary for accurate segmentation in medical images. In order to determine the suitable range of the parameter p, 20 ultrasound images of renal cysts and 20 CT images of HCC are randomly selected for experiments. The value interval of p is set to be [0.1,5]. By adopting selected values of p in the interval, we can get corresponding segmentation results that are subsequently calculated by the following Dice coefficients [42] to evaluate segmentation effects,

$$Dice = \frac{2(A \bigcap G)}{A \bigcap G + A \bigcup G}, \tag{12}$$

where A is the segmenting result and G is the ground truth.

Fig. 3. shows the average values of Dice for segmentation results in 20 ultrasound and CT images, respectively of using every selected p value. As can be seen, the accuracies of these results are satisfactory when p is between 0.5 and 3.7 for ultrasound images and CT images. The largest average values of dice for both types of images are obtained

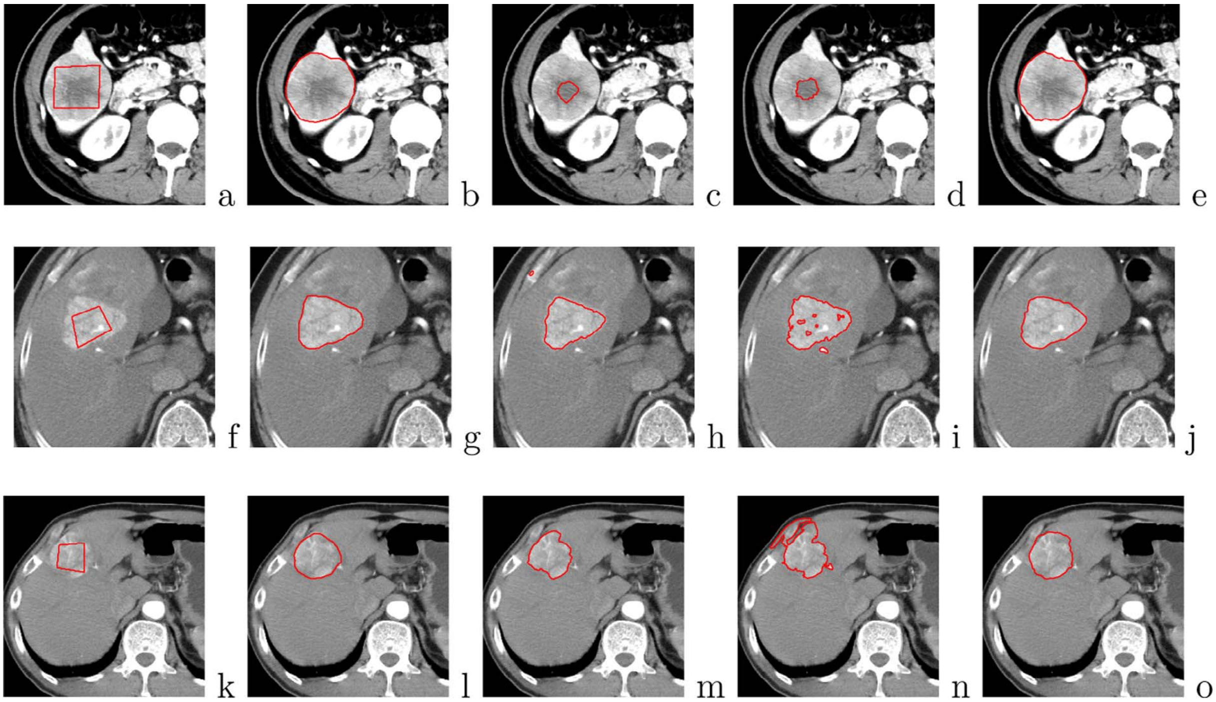

Fig. 7. Comparison results of CV model, BCS method and the proposed method on the CT images of HCC regions with blurred or/and partially missing boundaries. Same initializations are manually obtained for all methods in this comparison, and the initial contours are shown in the 1st. column; the 2nd. column: the ground truths; the 3rd. column: the results of the CV model; the 4th. column: the results of BCS method; the 5th. column: the results of our proposed method. Lesions in a, f, k are SN, SNEG and CM types, respectively.

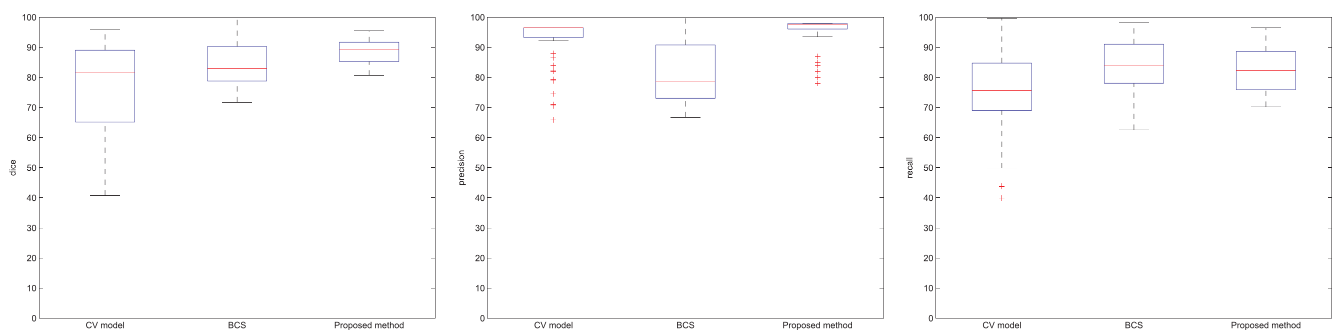

Fig. 8. The results of Dice, precision and recall (sensitivity) of the CV model, BCS method and the proposed method on 49 CT images of HCCs.

approximately at 2.8, which indicate the best segmentation results in this experiment. Therefore, we set $p = 2.8$ for all the following experiments.

4.3. Segmentation results and quantitative evaluations

Fig. 5. shows segmentation results of renal cysts in ultrasound images. Lesion regions are precisely segmented by using the proposed method. In order to evaluate the efficiency of the proposed method, two level set based segmentation methods, i.e., the classical CV model [30] and a region-based method for image segmentation and bias correction [39] (BCS method), are utilized for comparison. These comparison results demonstrate that the proposed method has a good performance for segmenting compact lesions in ultrasound images.

To quantitatively compare the segmentation results of three different methods, we use precision, recall and the Dice coefficient (as shown in (14)) as evaluation criteria [43]:

$$precision = \frac{TP}{TP+FP},$$
$$recall = \frac{TP}{TP+FN}, \tag{13}$$

where TP is the number of true positive pixels; TN is the number of true negative pixels; FP is the number of false positive pixels; and FN is the number of false negative pixels.

In this comparison, the ground truths of lesions are given by an experienced physician. Three compared methods adopt the same initialization curves and processing areas, which are automatically acquired from the previous detection procedure.

Fig. 6. shows the results of the quantitative comparison. As can be seen, the average Dice coefficient of the proposed method is 89.6%, and the average value of precision of our method reaches 96.0%. These results indicate that the proposed method has a good performance for segmenting compact lesions in ultrasound images and provide the segmentation results of renal cysts that are closer to the ground truths than those of two other methods.

The comparison is also carried out on 49 CT images of HCCs. Different from the previous experiments on renal cysts, the initialization contours are given manually. Fig. 7 shows the segmentation results of the proposed method and their comparison to the CV model and the BCS method. As can be seen, the segmentation results by using the proposed method are closer to the ground truths than those of other two methods. It is worthy noting that the shapes of HCC regions are various and irregular when compared with those of renal cysts. In clinical practice, surgically resectable HCCs can be subclassified into three

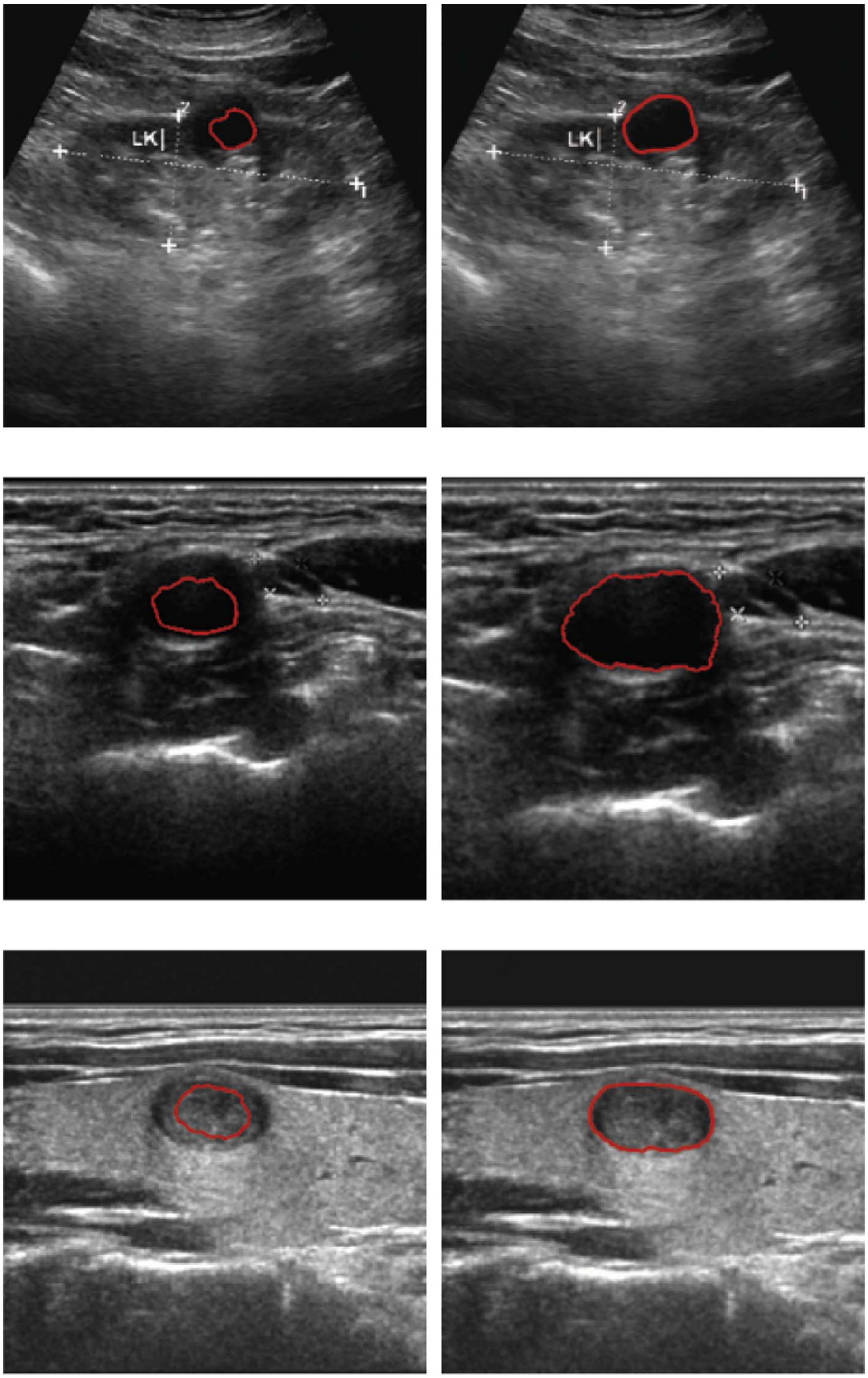

Fig. 9. Segmentation results in ultrasound images with automatic initializations. Left column: automatic initialization contours; right column: segmentation results. From top to bottom: a renal carcinoma with partially missing boundaries, an artery with partially missing boundaries, and a thyroid nodule with blurred boundaries.

types with distinctive morphologies: single nodular (SN) type, single nodular type with extranodular growth (SNEG), and confluent multinodular (CM) type [27]. In our experiment, although HCCs have irregular shapes, the lesion regions can be seen as relatively compact regions. As a result, they can be segmented precisely through the proposed method that is designed for segmentation of compact objects. This versatility is important for biomedical applications.

The quantitative comparison of these three methods is shown in Fig. 8. As can be seen, the average Dice coefficient of the proposed method is 88.7%, exhibiting the largest value among the coefficients of three methods. The average value of the precision of our method is 96.6%, which is also the highest. These comparison results demonstrate that the proposed method offers more precise segmentation results for HCCs in CT images in comparison with other tested methods.

In Fig. 5 and Fig. 7, the experimental results of classical CV model, the BCS method and the new approach in ultrasound images and CT images are presented. The proposed method performs to be more effective than other two methods on segmenting some medical images with challenges, including low contrast (e.g. Fig. 5(a), (e) and (k)), inhomogeneous intensities (e.g. Fig. 5(e), (a) and (f)), and blurred or/and partially missing boundaries (e.g. Fig. 5(i) and Fig. 7(k)).

In these comparisons, the number of iterations of these methods is 200. For the classical CV model, $h = \epsilon = 1.0, \Delta t = 0.1$ and the parameter for the arc length term is: $\nu = 10 \times 255 \times 255$. For the BCS method,

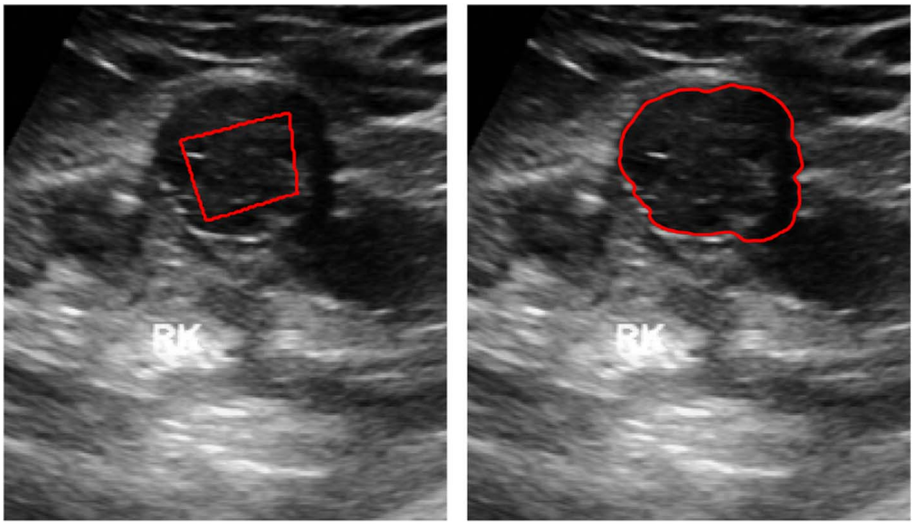

Fig. 10. An example of renal carcinoma in ultrasound image with inhomogeneity and partially missing boundaries. Left: the manual initialization curve, right: the segmentation result obtained by the proposed method.

$h = \epsilon = 1.0, \Delta t = 0.1$, the coefficient for the distance regularization term is: $\mu = 1$, and the scale parameter that specifies the size of the neighborhood is: $\sigma = 4$. For the proposed method, $h = \epsilon = 1.0, \Delta t = 0.1$, the coefficient for the shape energy term is: $\theta = 1$, and $p = 2.8$ according to the experimental results shown in Fig. 4.

All experiments are implemented in MATLAB R2012b on a personal computer with i5-5200U CPU, 2.20 GHz 8 GB RAM. The average execution time for the CV model, the BCS method, and the proposed method on these 101 images (52 ultrasound images and 49 CT images) are 0.52 s, 1.24 s and 1.26 s, respectively.

4.4. Segmentation of other types of medical images

Since the isoperimetric constraint is a compact shape constraint, the proposed method can also be used to segment other lesions with compact shapes in various medical images.

Fig. 9 shows the segmentation results of a renal carcinoma, an artery, and a thyroid nodule. For these objects, their initializations are obtained automatically by using the same detection approach for renal cysts. Notably, these objects in ultrasound images have various degrees of blurred or/and partially missing boundaries, but they can still be precisely segmented. Fig. 10 shows an ultrasound image of renal carcinoma having more inhomogeneous intensities and serious situation of partially missing boundaries. This lesion can also be segmented with the proposed method, which further confirms its effectiveness on compact lesions.

The proposed method is also effective on segmenting compact lesions in MR images. Fig. 11. shows the segmentation results of a renal angiomyolipoma with low contrast, a parotid mass with blurred boundaries, and a breast cancer with an irregular shape. As shown before, all these lesions are successfully segmented by the proposed method despite the presence of factors that would make segmentation challenging for conventional methods.

In order to establish the efficiency of the proposed method, except HCC, other two types of focal liver lesions, including focal nodular hyperplasias and hemangiomas, are also segmented in our experiments. some results are shown in Fig. 12. As can be seen in these cases, the shapes of the lesion regions are more compact and regular than those of HCC lesions. Moreover, human organs and structures with compact shapes can be segmented by the proposed method, some results are presented in Fig. 13. In this paper, the kidney, the prostate, and the left ventricle are tested, as we can see in these figures, the shapes of these organs are relatively regular. These experiments illustrate the general capability of the proposed method.

Finally, the segmentation of multiple objects in images is tested. As seen in Fig. 14, two regions with similar intensities in an ultrasound image are manually initialized as targets, which are consequently segmented by using the proposed method.

5. Discussions and conclusions

The effective segmentation of medical images is challenging, because the images may have heavy noise and intensity inhomogeneity and the objects may have blurred or/and partially missing boundaries. Prior knowledge is usually used to facilitate the segmentation of medical images. In this study, we propose a novel segmentation method by employing the general property of compactness, as many lesions and tissues present as compact shapes in medical images. We incorporate the compact shape constraint that is based on the isoperimentric inequality into the level set framework to propose a new energy functional. In combination with the intensity information from data terms, this proposed isoperimetric constraint can deal with the objects with blurred or/and partially missing boundaries.

The isoperimetric constraint based level set segmentation model has several advantages. Firstly, the length of the contour, the area inside the contour and the compactness of the shape are simultaneously controlled by this constraint. Secondly, the smoothness of the segmenting contour is also guaranteed, because the regularization term, which is the ratio of the squared perimeter to the enclosed area of the contour, gives a penalty to force the contour to become smooth. Thirdly, minimizing the ratio of the squared perimeter to the enclosed area of the segmenting region can ensure that blurred or/and partially missing boundaries are completed to form compact shapes. Fourthly, only one parameter p is used in the isoperimetric constraint. Experiments on ultrasound and CT images indicate that the value of p can be set in a large efficient range while it maintains accuracy and reliability of the segmentation. Compared to other shape prior based models, this proposed method has no need to estimate shape parameters or to train shapes. Lastly, the proposed method can segment objects with different sizes and shapes.

Theoretically, the initial contours are drove to the real boundaries by the data term and regularized by the isoperimetric constraint. So, generally speaking, there are no specific guidelines for the initialization of the segmentation algorithm. However, there are some exceptions, such as the target regions with strong inhomogeneity, in which special initializations are required to achieve accurate segmentation results. A typical example is the segmentation of the left ventricle, which is shown in Fig. 13, line 2, right. In this case, the desired segmentation contour should be located in the endocardium of the left ventricle. This requirement means that the cavity of the left ventricle (presented as grey

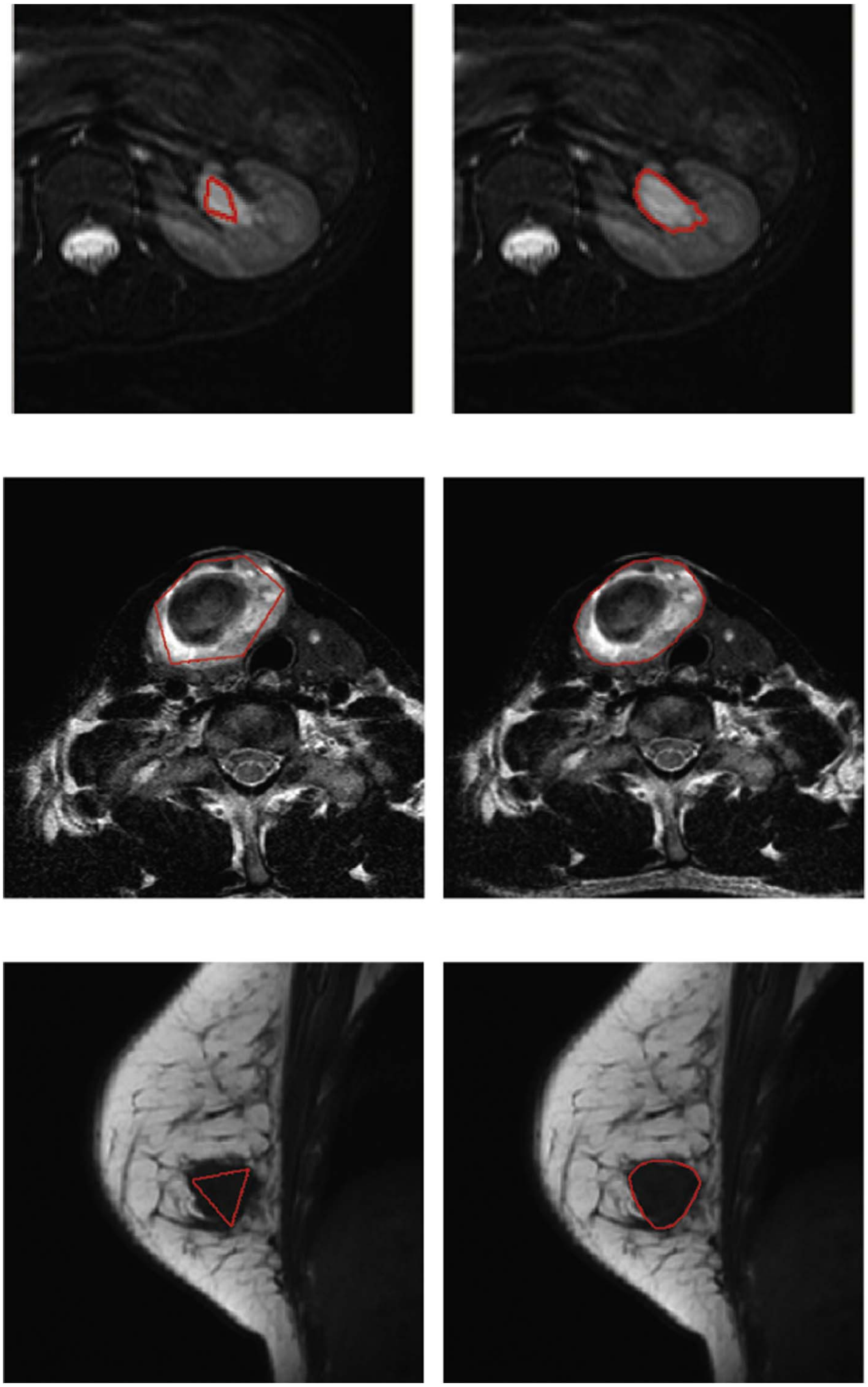

Fig. 11. Segmentation results of lesions in MR images. From top to bottom: a renal angiomyolipoma, a parotid mass, and a breast cancer. Left column: manual initialization curves; right column: segmentation curves obtained by using the proposed method.

or white region) and the papillary muscles (presented as black regions) should be segmented as an integrated target, and then both regions should be enclosed by the initial curve to ensure the precise segmentation result.

Considering that many lesions and organs have compact appearances in images, the isoperimetric constraint has wide applications in medical image segmentation. In this paper, experiments are implemented on various lesions and organs in different types of medical images, these accurate results prove the capability of the proposed method.

Admittedly there are some exceptions, like the hippocampus in brains and vessel systems in livers, these structures with specific shapes (i.e. shape like a hook or hippocampus, and shape like a tree, respectively) may not be regarded as compact shapes, and therefore these cases cannot be efficiently handled by the proposed method.

In conclusion, the proposed method is versatile for medical image segmentation. Owing to the advantages of the proposed method, accurate segmentation of compact lesions and organs can be achieved. Useful information of medical images such as localizations, boundaries and sizes can be accurately generated from the segmentation results. The obtained information is crucial for the subsequent diagnoses and therapies. Moreover, because the isoperimetric constraint is a priori constraint of compact shapes and based on the isoperimetric inequality in any Euclidean space $R^n (n \geqslant 2)$, the possible future work in this

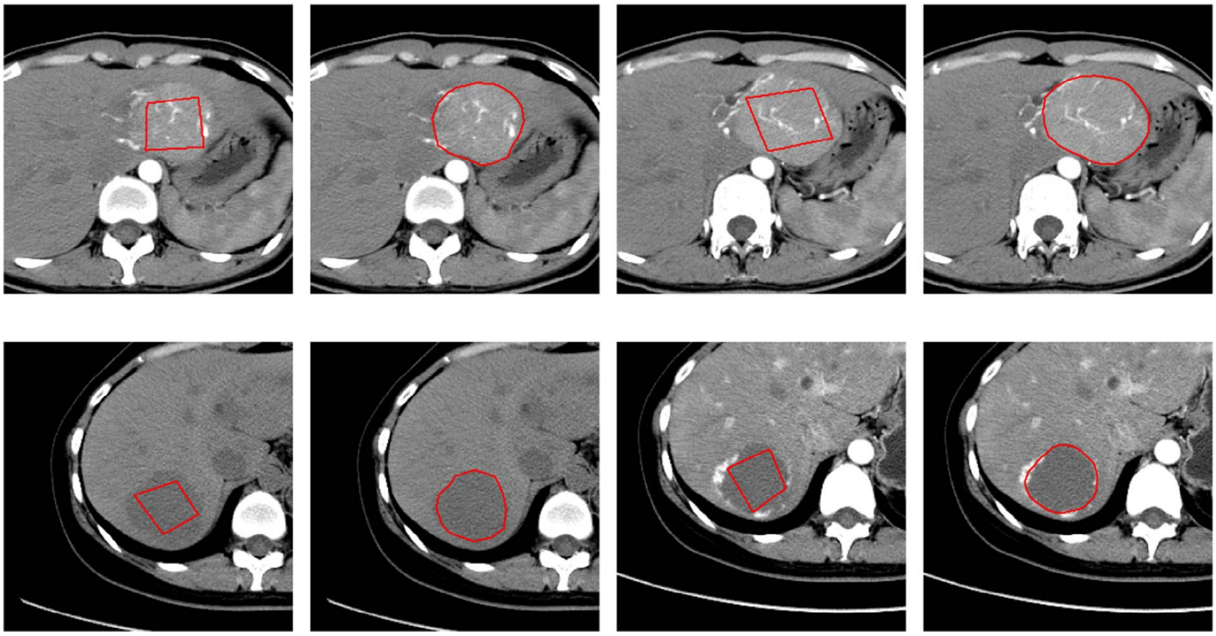

Fig. 12. Segmentation results of two types of focal liver lesions in CT images. The 1st line:focal nodular hyperplasias, and the 2nd line:hemangiomas. For each case, the manual initialization (left) and the segmentation result (right) are shown.

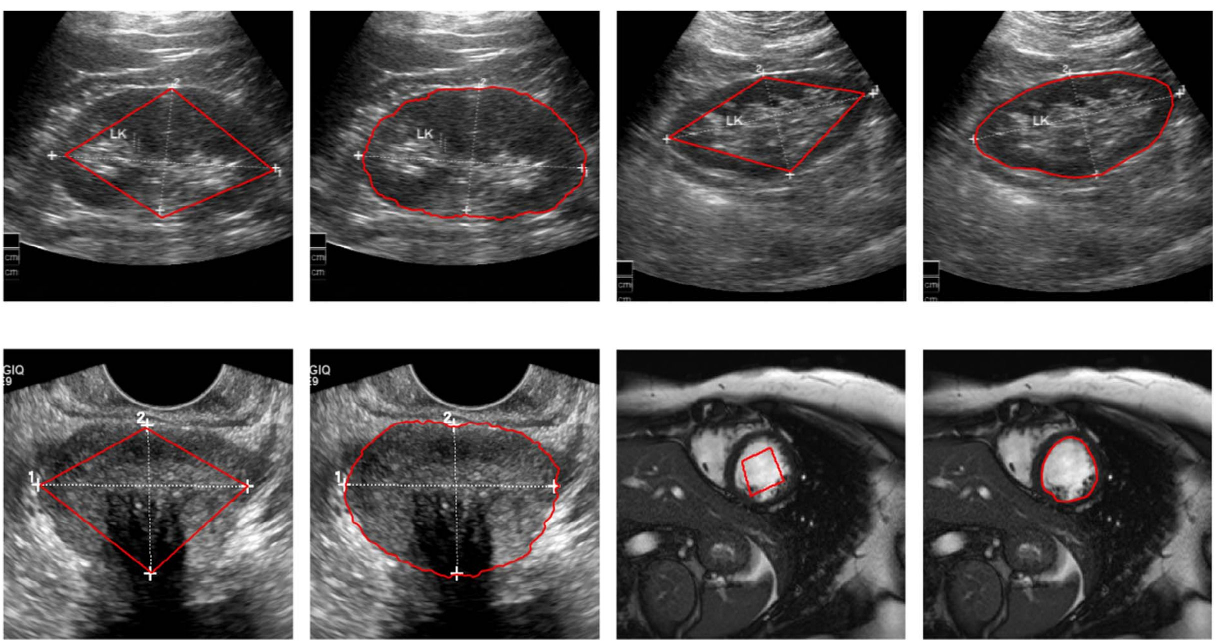

Fig. 13. Segmentation results of organs and structures in medical images. The 1st line: kidneys in ultrasound images, and the 2nd line: a prostate in ultrasound image and a left ventricle in MR image. For each case, the manual initialization (left) and the segmentation result (right) are shown.

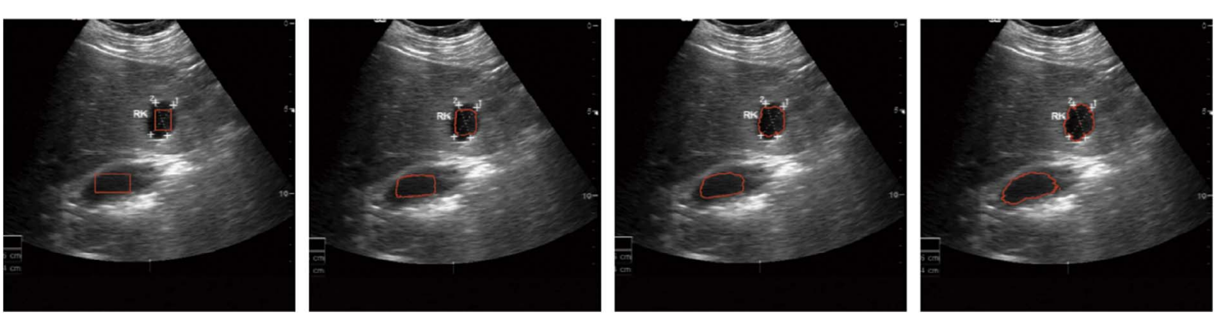

Fig. 14. Curve evolution of segmenting multiple objects in an ultrasound image. Images from left to right: the manual initialization: two rectangular initial curves are placed in two target regions, respectively; and the contours with iterations 20, 50, and 100.

aspect is to extend the proposed algorithm to segment 3D and more modality images, such as X-ray, positron emission tomography (PET) and optical coherent tomography (OCT) images.

Acknowledgments

This work is supported by National Nature Science Foundation of China (No. 11531005 and No. 91330101) and Natural Science Foundation of Jiangsu Province (BK20140965). The authors gratefully acknowledge Nanjing General Hospital and Nanjing Drum Tower Hospital, The Affiliated Hospital of Nanjing University Medical School for providing all the medical images used in this paper.

References

[1] Shen T, Li H, Huang X. Active volume models for medical image segmentation. IEEE Trans Med Imaging 2011;30(3):774–91.
[2] Spiegel M, Hahn DA, Daum V, Wasza J, Hornegger J. Segmentation of kidneys using a new active shape model generation technique based on non-rigid image registration. Comput Med Imaging Graphics 2009;33(1):29–39.
[3] Faisal Amir, Ng Siew-Cheok, Goh Siew-Li, George John, Supriyanto Eko, Lai Khin W. Multiple LREK active contours for knee meniscus ultrasound image segmentation. IEEE Trans Med Imaging 2015;34(10):2162–71.
[4] Perna L, Sini C, Cozzarini C, et al. Deformable registration-based segmentation of the bowel on Megavoltage CT during pelvic radiotherapy[J]. Physica Medica 2016;32(7):898–904.
[5] Noble JA, Boukerroui D. Ultrasound image segmentation: a survey. IEEE Trans Med Imaging 2006;25(8):987–1010.
[6] Carvalho DD, Akkus Z, van den Oord SC, Schinkel AF, van der Steen AF, Niessen WJ, Bosch JG, Klein S. Lumen segmentation and motion estimation in b-mode and contrast-enhanced ultrasound images of the carotid artery in patients with atherosclerotic plaque. IEEE Trans Med Imaging 2015;34(4):983–93.
[7] Gutiérrez-Becker B, Cośo FA, Huerta MEG, Benavides-Serralde JA, Camargo-Mańn L, Bañuelos VM. Automatic segmentation of the fetal cerebellum on ultrasound volumes, using a 3d statistical shape model. Med Biolog Eng Comput 2013;51(9):1021–30.
[8] Xie J, Jiang Y, Tsui H-T. Segmentation of kidney from ultrasound images based on texture and shape priors. IEEE Trans Med Imaging 2005;24(1):45–57.
[9] Qiu W, Yuan J, Ukwatta E, Sun Y, Rajchl M, Fenster A. Prostate segmentation: an efficient convex optimization approach with axial symmetry using 3-d trus and mr images. IEEE Trans Med Imaging 2014;33(4):947–60.
[10] Ali S, Madabhushi A. An integrated region-, boundary-, shape-based active contour for multiple object overlap resolution in histological imagery. IEEE Trans Med Imaging 2012;31(7):1448–60.
[11] Gloger O, Tönnies KD, Liebscher V, Kugelmann B, Laqua R, Völzke H. Prior shape level set segmentation on multistep generated probability maps of mr datasets for fully automatic kidney parenchyma volumetry. IEEE Trans Med Imaging 2012;31(2):312–25.
[12] Huang J, Yang X, Chen Y, Tang L. Ultrasound kidney segmentation with a global prior shape. J Visual Commun Image Represent 2013;24(7):937–43.
[13] Zeng YZ, Zhao YQ, Liao M, Zou BJ, Wang XF, Wang W. Liver vessel segmentation based on extreme learning machine. Physica Medica 2016;32(5):709–16.
[14] Liao M, Zhao YQ, Wang W, Zeng YZ, Yang Q, Shih FY, Zou BJ. Efficient liver segmentation in CT images based on graph cuts and bottleneck detection. Physica Medica 2016;32(11):1383–96.
[15] Liu B, Cheng H, Huang J, Tian J, Tang X, Liu J. Probability density difference-based active contour for ultrasound image segmentation. Pattern Recognit 2010;43(6):2028–42.
[16] Yang J, Duncan JS. 3d image segmentation of deformable objects with joint shape-intensity prior models using level sets. Med Image Anal 2004;8(3):285–94.
[17] Leventon ME, Grimson WEL, Faugeras O. Statistical shape influence in geodesic active contours. Proceedings IEEE Conference on Computer Vision and Pattern Recognition, 2000, vol. 1. IEEE; 2000. p. 316–23.
[18] Karasev P, Kolesov I, Fritscher K, Vela P, Mitchell P, Tannenbaum A. Interactive medical image segmentation using pde control of active contours. IEEE Trans Med Imaging 2013;32(11):2127–39.
[19] Brox T, Weickert J. Level set segmentation with multiple regions. IEEE Trans Image Process 2006;15(10):3213–8.
[20] Li C, Xu C, Gui C, Fox MD. Distance regularized level set evolution and its application to image segmentation. IEEE Trans Image Process 2010;19(12):3243–54.
[21] Malladi R, Sethian J, Vemuri BC, et al. Shape modeling with front propagation: a level set approach. IEEE Trans Pattern Anal Mach Intelligence 1995;17(2):158–75.
[22] Vukadinovic D, van Walsum T, Manniesing R, Rozie S, Hameeteman R, De Weert TT, Van der Lugt A, Niessen WJ. Segmentation of the outer vessel wall of the common carotid artery in cta. IEEE Trans Med Imaging 2010;29(1):65–76.
[23] Acho SN, Rae WID. Interactive breast mass segmentation using a convex active contour model with optimal threshold values. Physica Medica 2016;32(10):1352–9.
[24] Ray N, Acton ST, Ley K. Tracking leukocytes in vivo with shape and size constrained active contours. IEEE Trans Med Imaging 2002;21(10):1222–35.
[25] Chen Y, Tagare HD, Thiruvenkadam S, Huang F, Wilson D, Gopinath KS, Briggs RW, Geiser EA. Using prior shapes in geometric active contours in a variational framework. Int J Comput Vision 2002;50(3):315–28.
[26] Leventon ME, Faugeras O, Grimson WEL, Wells WM. Level set based segmentation with intensity and curvature priors. Proceedings IEEE Workshop on Mathematical Methods in Biomedical Image Analysis, 2000 IEEE; 2000. p. 4–11.
[27] Murakata A, Tanaka S, Mogushi K, Yasen M, Noguchi N, Irie T, Kudo A, Nakamura N, Tanaka H, Arii S. Gene expression signature of the gross morphology in hepatocellular carcinoma. Ann Surg 2011;253(1):94–100.
[28] Kim JW, Kim JH, Won HJ, Shin YM, Yoon HK, Sung KB, Kim PN. Hepatocellular carcinomas 2?C3cm in diameter: Transarterial chemoembolization plus radiofrequency ablation vs. radiofrequency ablation alone. Eur J Radiol 2012;81(3):e189–93.
[29] Ebara M, Okabe S, Kita K, Sugiura N, Fukuda H, Yoshikawa M, Kondo F, Saisho H. Percutaneous ethanol injection for small hepatocellular carcinoma: Therapeutic efficacy based on 20-year observation. J Hepatol 2005;43(3):458–64.
[30] Chan TF, Vese LA. Active contours without edges. IEEE Trans Image Process 2001;10(2):266–77.
[31] Chavel I. Isoperimetric inequalities: differential geometric and analytic perspectives vol. 145. Cambridge University Press; 2001.
[32] Veksler O. Stereo correspondence with compact windows via minimum ratio cycle. IEEE Trans Pattern Anal Mach Intell 2002;24(12):1654–60.
[33] Grady L, Schwartz EL. Isoperimetric graph partitioning for image segmentation. IEEE Trans Pattern Anal Mach Intell 2006;28(3):469–75.
[34] Grady L, Sun V, Williams J. Interactive graph-based segmentation methods in cardiovascular imaging. Handbook Math Models Comput Vision 2006:453–69.
[35] Bodur O, Grady L, Stillman A, Setser R, Funka-Lea G, O'Donnell T. Semi-automatic aortic aneurysm analysis. Medical imaging International Society for Optics and Photonics; 2007. p. 65111G.
[36] Grady L, Singh V, Kohlberger T, Alvino C, Bahlmann C. Automatic segmentation of unknown objects, with application to baggage security, Lecture Notes in Computer Science (including subseries Lecture Notes in Artificial Intelligence and Lecture Notes in Bioinformatics) 7573 LNCS (PART 2) (2012) 430–44.
[37] Koepfler G, Lopez C, Morel JM. A multiscale algorithm for image segmentation by variational method. SIAM J Numer Anal 1994;31(1):282–99.
[38] Zhao H-K, Chan T, Merriman B, Osher S. A variational level set approach to multiphase motion. J Comput Phys 1996;127(1):179–95.
[39] Li C, Huang R, Ding Z, Gatenby J, Metaxas DN, Gore JC. A level set method for image segmentation in the presence of intensity inhomogeneities with application to mri. IEEE Trans Image Process 2011;20(7):2007–16.
[40] Pallotta Nadia. Differential diagnosis in ultrasound imaging. Gastroenterology 2007;133(5):1740–1.
[41] Otsu Nobuyuki. A threshold selection method from gray-level histograms. IEEE Trans Syst Man Cybern 1979;20(1):62–6.
[42] Dice LR. Measures of the amount of ecologic association between species. Ecology 1945;26(3):297–302.
[43] Powers DM. Evaluation: from precision, recall and f-measure to roc, informedness, markedness & correlation. J Mach Learning Technol 2011;2(1):37–63.